Measurement of the ^{159}Tb(n, γ) cross section at the CSNS Back-n facility

S. Zhang,[1,*] G. Li,[1] W. Jiang,[2] D. X. Wang,[1] J. Ren,[3] M. Huang,[1,†] E. T. Li,[4] J. Y. Tang,[2] X. C. Ruan,[3] H. W. Wang,[5] Z. H. Li,[3] Y. S. Chen,[3] L. X. Liu,[5] X. X. Li,[6] Q. W. Fan,[3] R. R. Fan,[2] X. R. Hu,[6] J. C. Wang,[1,3] X. Li,[1] D. D. Niu,[1] N. Song,[1,3] and M. Gu[1]

[1]*College of Mathematics and Physics, Inner Mongolia Minzu University, Tongliao 028000, China*
[2]*Institute of High Energy Physics, Chinese Academy of Sciences, Beijing 100049, China*
[3]*China Institute of Atomic Energy, Beijing 102413, China*
[4]*Institute for Advanced Study in Nuclear Energy and Safety, College of Physics and Optoelectronic Engineering, Shenzhen University, Shenzhen 518060, China*
[5]*Shanghai Advanced Research Institute, Chinese Academy of Sciences, Shanghai 201210, China*
[6]*Shanghai Institute Applied Physics, Chinese Academy of Sciences, Shanghai 201800, China*

(Received 5 December 2022; accepted 10 April 2023; published 26 April 2023)

The stellar (n, γ) cross section data for the mass numbers around $A \approx 160$ are of key importance to nucleosynthesis in the main component of the slow neutron capture process, which occurs in the thermally pulsing asymptotic giant branch (TP-AGB). The new measurement of (n, γ) cross sections for ^{159}Tb was performed using the C_6D_6 detector system at the back streaming white neutron beam line (Back-n) of the China spallation neutron source with neutron energies ranging from 1 eV to 1 MeV. Experimental resonance capture kernels are reported up to 1.2 keV neutron energy with this capture measurement. Maxwellian-averaged cross sections (MACS) are derived from the measured ^{159}Tb(n, γ) cross sections at kT = 5–100 keV and are in good agreement with the recommended data of KADoNiS-v0.3 and JEFF-3.3, while KADoNiS-v1.0 and ENDF-VIII.0 significantly overestimate the present MACS up to 40% and 20%, respectively. A sensitive test of the s-process nucleosynthesis is also performed with the stellar evolution code MESA. Significant changes in abundances around $A \approx 160$ are observed between the ENDF/B-VIII.0 and present measured rate of ^{159}Tb(n, γ) ^{160}Tb in the MESA simulation.

DOI: 10.1103/PhysRevC.107.045809

I. INTRODUCTION

The elements heavier than iron in the solar system are mainly produced by the slow neutron capture process (s process) [1] and the rapid neutron capture process (r process) [2] in stars as found by Burbidge *et al.* [3] and Cameron [4] as early as 1957. Almost less than 1% of heavy elements are ascribed to the production of photodisintegration processes (the so-called p/γ process), neutrinos, and charged-particle induced reactions [5,6]. The s process takes place during stellar evolution and path through nuclei along the valley of β stability with lower neutron densities and temperatures. The weak s process is responsible for producing isotopes up to $A \approx 90$ and occurs during He and C burning in massive stars. While the main s process contributes isotopes $A \approx 90$–208 and takes place in the thermally pulsing asymptotic giant branch (TP-AGB) phase of low- and intermediate-mass stars. The r process is related to explosive nucleosynthesis in massive stars and binary star mergers with relatively high neutron densities.

Terbium is mainly produced by the explosive r process [2], while about 9% is made by main s process in low- and intermediate-mass TP-AGB stars [7]. The s-process reaction path around terbium is sketched in Fig. 1. ^{160}Tb is an important s-process branching point, which is shielded against the β^- decay chains from the r process by stable nuclei ^{160}Gd. The abundance of ^{160}Tb will affect the s-only isotope ^{160}Dy, which paths through the s process to ^{161}Dy and considered as an reference point for the reaction flow. Also, neutron capture of terbium isotopes will contribute to the production of p-nuclei ^{164}Er through the temperature sensitive branching at ^{163}Dy to ^{163}Ho by the nuclear reaction path ^{163}Ho(n, γ) ^{164}Ho(β) ^{164}Er in the stellar environment [8–10].

Two groups of experimental neutron capture cross section data for ^{159}Tb(n, γ) reaction were reported between 1961 and 1991 [11–16] in the astrophysical interested energy region. Data from Block *et al.* [11], Gibbons *et al.* [12], Lépine *et al.* [13] are significantly larger than data of Mizumoto *et al.* [14], Ohkubo *et al.* [15], and Bokhovko *et al.* [16]. In the KADoNiS-v0.3 [17] database, the recommended Maxwellian-averaged cross sections (MACS) of ^{159}Tb(n, γ) at stellar temperature kT = 30 keV is 1580 ± 150 mb, which is widely used in stellar nucleosynthesis calculations, derived from the neutron capture cross section data of Mizumoto *et al.* [14] and Bokhovko *et al.* [16]. While, this value reported by the recent activation measurement [18] with 2166 ± 181 mb and it varies from 1116 to 2949 mb in the collection list of the KADoNiS-v1.0 [19] and references therein. Because of

*zsylt@imun.edu.cn
†huangmeirong@imun.edu.cn

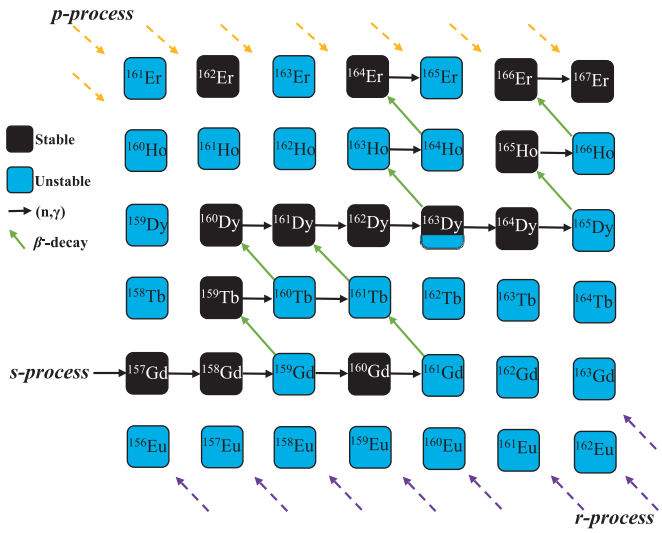

FIG. 1. The *s*-process reaction path in the region of terbium. Black solid boxes indicate stable; blue empty boxes indicate unstable isotopes. Arrows to the right and the next higher elements represent neutron capture reactions and β^- decays, respectively. The isotope ^{163}Dy is a terrestrially stable nucleus, which becomes unstable at stellar temperature [8].

such large discrepancies, newer measurements of stellar neutron capture cross section of ^{159}Tb are desired for improving the reliability of recommended data. Much higher accurate neutron capture cross sections for the terbium isotopes are required for the *s*-process nucleosynthesis, and the separation of the *r* and *s* components in the observed Tb abundance through subtraction of the *s* abundances from the respective solar values. In addition, the ^{159}Tb(n,γ) cross section data are very important for the design of the nuclear reactor and research in nuclear structure [20,21].

In the past years, a series of neutron radiative capture experiments have been performed using the C_6D_6 detectors (where 'D' denotes deuterium, '^{2}H') with the total energy technique [22–26] and the total absorption calorimeter consists of BaF_2 scintillator arrays [24,27–29] in combination with the ^{7}Li$(p,n)^7$Be reaction neutrons and white neutron sources. Both of the C_6D_6 and BaF_2 detection systems, respectively, were constructed at the back streaming white neutron facility (Back-n) of the China Spallation Neutron Source(CSNS) [30,31], which is the only high intense pulsed spallation reaction neutron source in China at present. The main physics motivation of these systems is to measure the neutron capture data related to the nuclear astrophysics, advanced nuclear energy technologies such as accelerator-driven subcritical systems, thorium-based molten salt reactor, and fourth generation reactors. The detection systems, experimental techniques, background study, and resonance energy region measurements have been described in Refs. [32–35]. In this work, we report on the experiment of neutron capture cross sections for ^{159}Tb over the energy range from 1 eV to 1 MeV via the time-of-flight (TOF) method combined with the white neutron beam at the CSNS Back-n facility. The resonance kernels of ^{159}Tb(n,γ) are obtained up to 1.2 keV, and the MACS for the astrophysical interest energy region from $kT = 5$–100 keV are calculated.

TABLE I. Characteristic parameters of samples.

Sample	Thickness (mm)	Diameter (mm)	Mass (mg)	Area desity (atom b^{-1})
^{nat}Tb	0.20	30	1169.14	6.27×10^{-4}
^{197}Au	0.10	30	1357.17	5.87×10^{-4}
^{nat}Pb	0.53	30	4249.75	1.75×10^{-3}
Empty holder				

II. EXPERIMENT

The measurement of ^{159}Tb(n,γ) was performed at the CSNS Back-n facility [30,31] in China. Neutrons were produced via the spallation reactions by bombarding a massive tungsten target with a 1.6 GeV proton beam, operating at a 25 Hz repetition rate, and collimated to a 30 mm diameter beam spot at the sample position. The neutron energies ranging from thermal to a few hundred MeV were determined using the time of flight (TOF) method with a 76 m long flight path. The neutron capture yields were studied using the total energy measurement principle based on an array of four C_6D_6 detectors with the pulse height weighting techniques (PHWT) [36–38]. The neutron flux in the energy range of 1 eV to 100 MeV was obtained with a combination of the data from dedicated measurements of the ^{6}LiF-silicon (Li-Si) detector array [39] and the ^{235}U loaded multilayer fission chamber [40]. The Li-Si detector neutron flux was normalized to ^{235}U data at 10–20 keV since its position was about 20 m away from the sample. The samples used for this experiment are listed in Table I. A metallic terbium sample of natural abundance with a thickness of 0.2 mm was used for the ^{159}Tb(n,γ) reaction study. The ^{197}Au sample was used as the standard for calculating the relative cross section of ^{159}Tb(n,γ) in neutron energies ranging from 2 keV to 1 MeV. The ^{nat}Pb samples were used to normalize the neutron fluence and to evaluate the in-beam γ rays and scattered-neutron backgrounds, respectively. The empty sample runs were also performed to evaluate the background produced from the upstream devices, such as the sample holders, etc. All experimental data were collected on an event-by-event basis high-performance data acquisition system with a 12-bit full-waveform digitizers sampling at 1 GS/s [41]. The offline data analysis was done on the CERN ROOT framework [42].

III. DATA ANALYSIS AND RESULTS

The incident neutron energy E_n was determined by employing the TOF method through the nonrelativistic kinematics formula (1). The neutron effective flight path L was obtained by analyzing the low energy resonances of the gold sample:

$$E_n = \left(\frac{72.2977 \times L}{t_n}\right)^2, \tag{1}$$

where E_n is in MeV, L is in meters, and t_n is the flight time in ns.

The experimental neutron capture yield as a function of E_n can be calculated as:

$$Y_{\rm exp}(E_n) = \frac{1}{f}\frac{C^w(E_n) - B^w(E_n)}{\Phi(E_n) \times E_c} \quad (2)$$

where f is the normalization factor determined by self-normalizing the measured capture yield of 4.9 eV resonance of ^{197}Au and 11.1 eV resonance of ^{159}Tb, based on the saturated resonance technique [43,44]. E_c is the detection efficiency for a capture event, $\Phi(E_n)$ is the neutron flux spectrum, and $C^w(E_n)$ and $B^w(E_n)$ are the weighted count spectrum and the total background spectrum, respectively.

The PHWT method is essential for the (n,γ) cross section measurement using the C_6D_6 detection system. Its function is to make the detection efficiency ε_γ proportional to the incident γ ray energy E_γ, as

$$\varepsilon_\gamma = \sum_{i=1}^{n} WF_i(E_d)R(E_d, E_\gamma) = \alpha E_\gamma, \quad (3)$$

where α is the constant parameter, R is the detector response function, E_d is the energy bin of pulse height spectrum, and WF is the weighting function, which can be approximated by a fifth polynomial function. The polynomial coefficients are obtained with a minimum least-squares fit to the the detector response for 27 different monoenergetic γ rays from 0.1 MeV to 10 MeV simulated by the GEANT4 code [45], taking into account the detailed model of the detection systems and the sample.

The background consists of two components, sample-independent and sample-dependent ones. The former is evaluated by the empty sample runs under the same experimental conditions. The sample-dependent background is mainly induced by in-beam γ rays and scattered neutrons on the sample. Their contributions were determined by measurements with a $^{\rm nat}$Pb sample and parametrized as

$$B(E_n) = f_\gamma B_\gamma(E_n) + f_n B_n(E_n), \quad (4)$$

where the B_γ and B_n denote the background contribution of the in-beam γ rays and scattered neutrons, respectively, and can be formulated as

$$B_\gamma(E_n) = b \times e^{-c/\sqrt{E_n}} + d \times e^{-e\times\sqrt{E_n}} + f, \quad (5)$$

$$B_n(E_n) = \frac{a}{\sqrt{E_n}}. \quad (6)$$

In order to normalize these background components, B_γ and B_n, dedicated runs with the ^{181}Ta and ^{59}Co neutron filters were performed. Figure 2 shows the energy spectrum obtained from ^{159}Tb with filters and background components. The normalization factors f_n and f_γ for B_n and B_γ components were obtained by matching the dips of the filtered spectra. The effect of the filters on in-beam γ rays and neutrons is evaluated by considering the neutron flux and energy distribution of in-beam γ rays. The neutron and γ energy spectra of Back-n are sampled for the incident particle energy spectra using the GEANT4 code to simulate with and without filters, and the counts of scattered neutrons and γ are recorded at the detector position [32]. The reduced neutron and γ attenuation factors

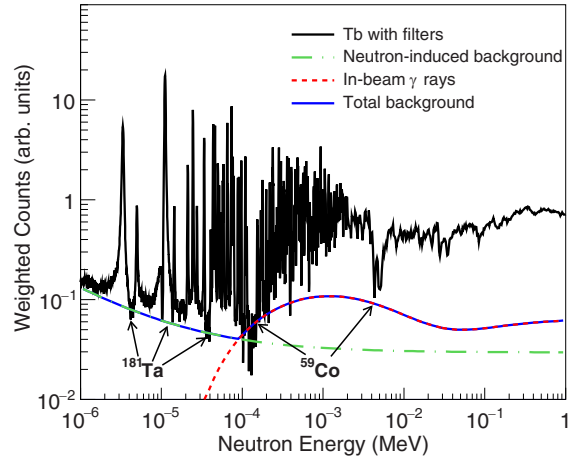

FIG. 2. ^{159}Tb(n,γ) capture yield with filters and background components are shown as a function of neutron energy. Black and blue solid lines indicate the ^{159}Tb sample with ^{181}Ta + ^{59}Co neutron filters and total background which is made of scattered neutrons (green dash-dotted lines) and in-beam γ rays (red dashed lines).

are 0.92 and 0.68, respectively, and are used for corrections to f_n and f_γ.

The resonance parameters (i.e., the radiative width Γ_γ and the neutron width Γ_n) are extracted using the R-matrix code SAMMY [46] to fit the experimental capture yields of ^{159}Tb(n,γ) in the resonance region up to 1.2 keV with the JEFF-3.3 [47] evaluated data as initial values. The code includes the experimental conditions, such as sample composition, multiple scattering, neutron self-shielding, and the Doppler effect at room temperature. The energy-dependent parametrized resolution function of the Back-n facility [48] is used to broaden the resonance peaks. The measured capture yields together with the SAMMY fits in neutron energy ranges below 100 eV are shown in Fig. 3. Good agreements were observed between present data and SAMMY fits both in the resonance energy and shape. The resonance parameters obtained in this work are compared with those from JEFF-3.3 evaluations given in the Appendix. The experimental capture resonance parameters show substantial agreement with the JEFF-3.3 evaluations in the energy range below 100 eV. However, differences are noted in the energy range between 100 eV and 1.2 keV, which is attributed to the degradation of the experimental resolution of the Back-n facility in this measurement. Average resonance parameters (such as the average level spacing, the neutron strength functions, the average radiation widths) are determined by fitting the measured average capture cross section data in the energy range between 2 keV and 200 keV with the code FITACS [49], implemented in SAMMY. The resonance parameters given by Mughabghab [50] are used for initial values in the fitting procedure and the average level spacing is specified as 3.78 eV [50]. The results obtained from the FITACS fit and the recommended data [50,51] are given in Table IX.

The measured neutron capture cross section ratio of ^{159}Tb relative to the standard ^{197}Au sample is obtained in the neutron energy range of 2 keV to 1 MeV using the same method as

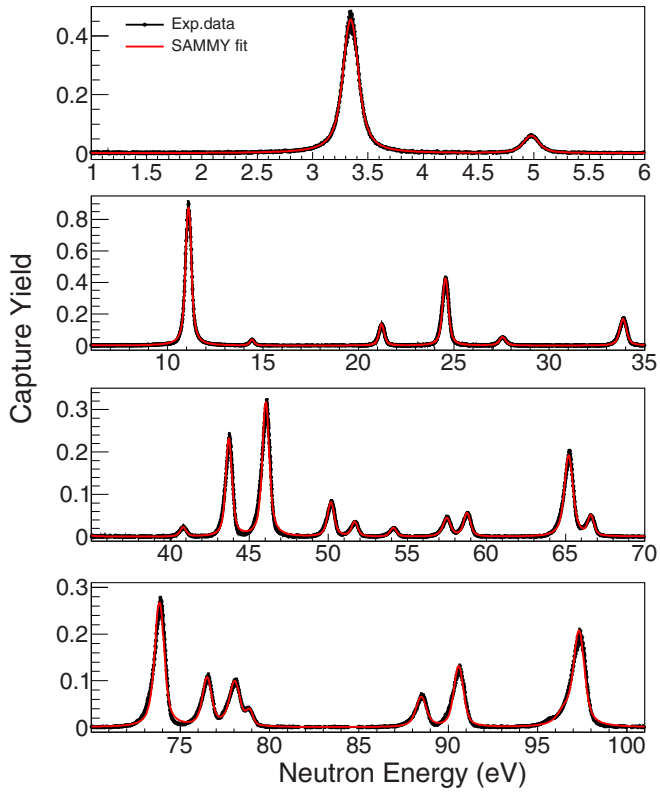

FIG. 3. The SAMMY fits to the experimental capture yields of ^{159}Tb(n,γ).

Refs. [28,52]. The absolute cross sections are converted from these ratios using the gold data of JEFF-3.3 evaluations. In Fig. 4, the experimental ^{159}Tb(n,γ) cross section and TALYS-1.9 [53] calculation result of this work are compared with the available measured data in literature [11–16] and evaluated data in libraries JEFF-3.3 [47], ENDF/B-VIII.0 [51]. As illustrated, the present experimental results are in good

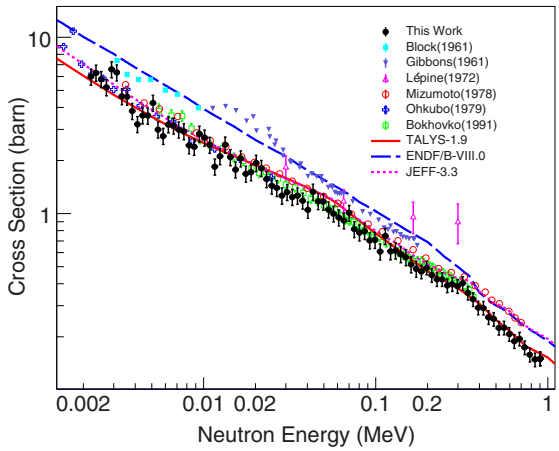

FIG. 4. Comparisons of the measured neutron capture cross section on ^{159}Tb of this work (black full circles) with previous measurements [11–16] (symbols), evaluations [47,51] (dashed lines), and TALYS-1.9 calculations [53] in the 2 keV to 1 MeV energy region.

TABLE II. The contributions from JEFF-3.3 evaluated data to present MACS.

kT (keV)	5	10	20	30	40	50	60	70	80	100
Ratio (%)	10.0	4.0	1.5	0.85	0.56	0.41	0.32	0.28	0.21	0.15

agreement with the data from TALYS-1.9, Bokhovko *et al.* [16] and Ohkubo *et al.* [15] in the overlapping energy regions. The cross section of JEFF-3.3 and Mizumoto *et al.* [14] are best fitted by the present data below 400 keV neutron energy and slightly larger above 400 keV. On the other hand, the data of Block *et al.* [11], Gibbons *et al.* [12], Lépine *et al.* [13], and ENDF/B-VIII.0 library are significantly overestimated result of this work.

The Maxwellian-averaged cross sections (MACS) for stellar temperature can be calculated from the neutron capture cross sections using the formula (7) [23,29]

$$\mathrm{MACS} = \frac{2}{\sqrt{\pi}(kT)^2}\int_0^\infty \sigma(E)Ee^{-E/kT}dE, \qquad (7)$$

where kT is stellar temperature, $\sigma(E)$ is the neutron capture cross section, E is the neutron energy.

For ^{159}Tb(n,γ), the present MACS are determined using three parts of cross sections from the 1 eV to 1 MeV energy range. The first part, shown in Fig. 5(a), is the cross sections reconstructed from the SAMMY fits to the present measured neutron capture yield in the resolved resonance region below 100 eV. The second part, shown in Fig. 5(b), is derived from the JEFF-3.3 evaluated cross section data between 100 eV and 2 keV since the resonance parameters obtained in this study are not sufficiently reliable due to the degradation of the experimental resolution. The JEFF-3.3 data contributions to the whole MACS are found in Table II. As we can see, this component cannot be ignored in the current study of *s*-process nucleosynthesis. The last part is provided by the present experimental cross sections relative to the gold standard over the energy range of 2 keV to 1 MeV as shown in Fig. 5(c).

The result of this work at $kT = 30$ keV is compared with previous experiments, theoretical calculations, and recommended data from the KADoNis database in Table III. The MACS recommended data from KADoNiS-v0.3 and the calculations of the TALYS-1.9 code agree with the present measured data less than 4%. The values from the recent activation measurement of Praena *et al.* [18], and the earlier data of Allen *et al.* [54], Lépine *et al.* [13] are relatively larger than the present result, whereas the results of Bokhovko *et al.* [16] and NON-SMOKER [57] are smaller. Theoretical calculations from MOST 2002 [56] and MOST 2005 [55] are obviously overestimated and underestimated by 89% and 28%, respectively, compared to the present data.

The MACS values are better to be known as a function of thermal energies between a few to a hundred keV at the various *s*-process sites. For completeness, the comparisons of the experimental MACS and the TALYS-1.9 calculation result of this work to the recommended data of KADoNis and

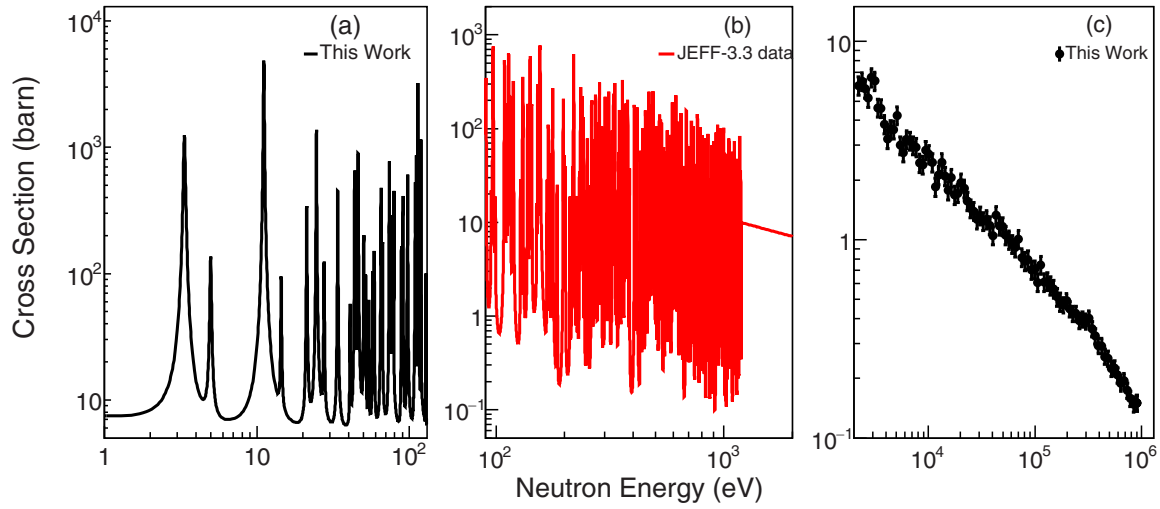

FIG. 5. The ^{159}Tb(n,γ) cross sections used in the calculation of present MACS.

evaluation libraries for stellar thermal energy from 5 to 100 keV are shown in Fig. 6 and Table IV. In the top panel, the black full circles and red solid line denote the present measured data and TALYS-1.9 calculation, respectively; the open green squares and blue circles indicate KADoNis-v0.3 and KADoNis-v1.0 recommended data; the blue dashed line and pink dotted line refer to calculated MACS by using the evaluated cross section data of ENDF/B-VIII.0 and JEFF-3.3 libraries. In the bottom panel, the ratios of the measured MACS to those from KADoNis-v0.3 (green open squares), KADoNis-v1.0 (blue open circles), ENDF/B-VIII.0 (blue dashed line), TALYS-1.9 (red solid line), and JEFF-3.3 (pink dotted line) data; black solid line corresponds to ratio 1. Our measured MACS data are well reproduced by the TALYS-1.9 calculation and the JEFF-3.3 evaluation less than 5% for the entire thermal energies studied. While, the present MACS is significantly smaller than those of the ENDF/B-VIII.0 evaluation by 30%–40%. It should be noted that, the present experimental MACS is smaller than KADoNiS-v0.3 data by about 3%–11% and 4% for the energy region $kT < 20$ keV and 20 keV $< kT <$ 100 keV, respectively. MACS data derived from KADoNis-v1.0 is larger about 15%–25% than the values of this work in the whole energy range.

The total experimental uncertainties of MACS include statistical and systematic contributions as shown in Table V. The statistical uncertainty is less than 1% below 100 eV and less than 5% between 2 keV and 1 MeV. The systematic uncertainties are due to neutron flux (4.5% below 150 keV and 8.0% above 150 keV), saturated resonance peak normalization (1%), background subtraction with filters (8.6%), flight path (0.08%, neglected), PHWT calculation (3%), and sample impurity (0.01%). Additionally, the contributions from neutron inelastic to the present MACS are included at different stellar temperatures as shown in Table VI, which cannot be eliminated in the present experiment.

The astrophysical reaction rates at a given thermal temperature can be numerically calculated from corresponding MACS as

$$N_A < \sigma v > (kT) = N_A \times \text{MACS} \times v, \tag{8}$$

where N_A is the Avogadro number, MACS is defined by Eq. (7), $v = \sqrt{2kT/\mu}$ is the mean thermal velocity. The ^{159}Tb(n,γ) rate of this work is fitted as a function of temperature T_9 (in units of 10^9 K) with the standard form of REACLIB:

$$\begin{aligned} N_A < \sigma v >_{(n,\gamma)} = \exp\big(&16.7928 + 0.0115 T_9^{-1} - 1.1836 T_9^{-1/3} \\ &+ 4.0069 T_9^{1/3} - 0.5127 T_9 + 0.03145 T_9^{5/3} \\ &- 1.3577 \ln T_9\big) \end{aligned} \tag{9}$$

with the fitting errors are less than 1% in the range from $T_9 = 0.02$ to $T_9 = 10$.

IV. ASTROPHYSICAL IMPLICATIONS

In TP-AGB stars, the ^{13}C pocket is formed following the third dredge-up (TDU) via ^{12}C$(p,\gamma)\,^{13}$N$(\beta^+\nu)\,^{13}$C and

TABLE III. The present MACS (in mb) of ^{159}Tb(n,γ) at $kT = 30$ keV compared to past experiments, calculations, and evaluations.

This work	1560 ± 160	KADoNis-v0.3 [17]	1580 ± 150	KADoNiS-v1.0 [19]	1817 ± 258
Praena 2014 [18]	2166 ± 181	Bokhovko 1992 [16]	1471 ± 66	Lépine 1972 [13]	1850 ± 250
Allen 1971 [54]	2200 ± 200	MOST 2005 [55]	1116	MOST 2002 [56]	2949
NON-SMOKER [57]	1427	TALYS-1.9 [53]	1628		

TABLE IV. The derived MACS for ^{159}Tb(n,γ) in mb.

kT (keV)	This work	KADoNis-v0.3 [17]	KADoNiS-v1.0 [19]	TALYS-1.9 [53]	ENDF/B-VIII.0 [51]	JEFF-3.3 [47]
5	4131 ± 421	4365	4875 ± 851	3892	5726	4028
10	2814 ± 287	2930	3323 ± 573	2790	3893	2750
15	2262 ± 231	2330	2664 ± 431	2294	3092	2232
20	1937 ± 198	2010	2276 ± 348	2014	2623	1927
25	1715 ± 175	1750	2012 ± 295	1792	2307	1716
30	1551 ± 158	1580 ± 150	1817 ± 258	1635	2076	1559
40	1318 ± 134	1340	1544 ± 211	1395	1756	1334
50	1159 ± 118	1185	1358 ± 181	1225	1540	1178
60	1041 ± 106	1070	1220 ± 159	1098	1381	1063
80	877 ± 91	910	1029 ± 128	920	1158	902
100	766 ± 82	800	898 ± 106	811	1005	794

generate neutrons by reaction ^{13}C(α,n) that trigger the *s* process [58–60]. The impact of ^{159}Tb stellar neutron capture cross sections on main *s*-process nucleosynthesis was investigated using the stellar evolution code MESA [61]. The stellar structure evolution and the *s*-process nucleosynthesis are computed with the MESA *star* and *net* modules separately, hence they require less computing time and resources. A low mass star with initial mass $2M_{\odot}$ and metallicity $Z = 0.01$ evolved from the premain sequence to near the end of the TP-AGB phase with nuclear network agb.net. In the ^{13}C pocket formed after the third TDU episodes, the temperature varies within 5.5–8.9 × 10^7 K and the density increase from 96.0 g/cm^3 to 7.7 × 10^3 g/cm^3 during the whole interpulse phase.

To treat the *s* process, detailed nucleosynthesis calculations were performed with the MESA *net* module. The network include 775 isotopes and 7344 reactions, and the temperature, density, and light nuclei initial abundance are extracted from the ^{13}C pocket of the precalculated stellar structure. The reaction rates corresponding to all proton, α, β decay, and neutron capture are provided by JINA REACLIB data tables, based on the 2017 updated version of the compilation by Cyburt *et al.* [62]. In addition, the initial element abundances are taken from Lodders *et al.* [63] for both structure and nucleosynthesis simulations.

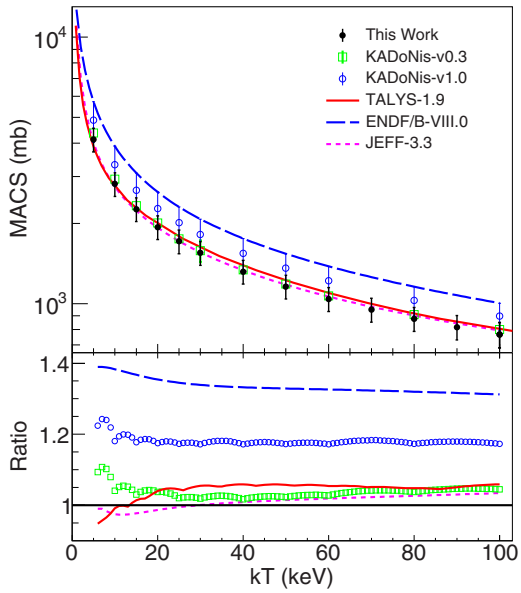

FIG. 6. (top) The MACS of ^{159}Tb(n,γ) and (bottom) the ratios between present experimental data and others [17,19,47,51].

The sensitivity of nuclear yields is evaluated to the reaction rate of ^{159}Tb$(n,\gamma)^{160}$Tb. Figure 7(a) shows the time evolution of the abundances of nuclides around $A \approx 160$ along the *s*-process reaction path at constant temperature ($T = 8.9 \times 10^7$ K) and density ($\rho = 7.7 \times 10^3$ g/cm^3) with the default case of the JINA REACLIB rate for ^{159}Tb$(n,\gamma)^{160}$Tb, which is derived from the KADoNiS-v0.3 database. The abundance of ^{163}Dy, which has a half-life of about 50 d in stellar environment [64], decreases rapidly due to the considering β-decay process to ^{163}Ho. The abundances of seed nuclei with initial values around $A \approx 160$ decreased significantly by neutron capture reactions before evolving to 7×10^{10} s because of the *s*-process flow from the dominant seed nuclei ^{56}Fe not yet overcoming the first *s*-process peak nuclei Sr and Ba, which act as bottlenecks in the reaction flow. On the other hand, the abundances of ^{160}Dy and ^{164}Er increased obviously with the depletion of ^{160}Tb and ^{163}Ho from about 10^7–4×10^9 s. Then, the productions of all nuclides around $A \approx 160$ increase continuously up to 2–3 orders larger than initial values at the end of interpulse. Figure 7(b) shows the abundance changes

TABLE V. Systematic uncertainties of MACS ^{159}Tb(n,γ) cross sections.

Source	Uncertainty (%)
Neutron flux (<150 keV; >150 keV)	4.5; 8.0
Pulse height weighting functions	3.0
Background subtraction with filters	8.6
Normalization factor	1.0
Flight path	0.08
Sample impurities	0.01
Total (without inelastic contribution)	10.2;12.2

TABLE VI. The contributions from neutron inelastic to present MACS.

kT (keV)	5	10	20	30	40	50	60	70	80	100
Ratio (%)	10^{-21}	10^{-11}	10^{-5}	10^{-3}	10^{-2}	0.21	0.68	1.61	3.11	7.90

between the KADoNiS-v0.3 and the ENDF/B-VIII.0 rate of ^{159}Tb$(n,\gamma)^{160}$Tb used in the network calculations. In this case, the data of KADoNiS-v0.3 are smaller by about 40% than that of ENDF/B-VIII.0. The abundances of ^{159,160}Tb, ^{160,161}Dy noticeably are affected by the uncertainty of the cross section of the ^{159}Tb$(n,\gamma)^{160}$Tb reaction. While, these propagation effects are less important for those nuclei heavier than ^{159}Tb. This trend is caused by achieving s-process reaction flow equilibriums [1,65,66] due to the high neutron fluence in the ^{13}C pocket. Figure 7(c) shows the same physical quantities as in Fig. 7(b) but with the ^{159}Tb$(n,\gamma)^{160}$Tb rate of this work instead of the ENDF/B-VIII.0 data in calculations. As shown in the figure, the changes of abundances are much smaller than those of Fig. 7(b) because of good agreement between two rates within 5%.

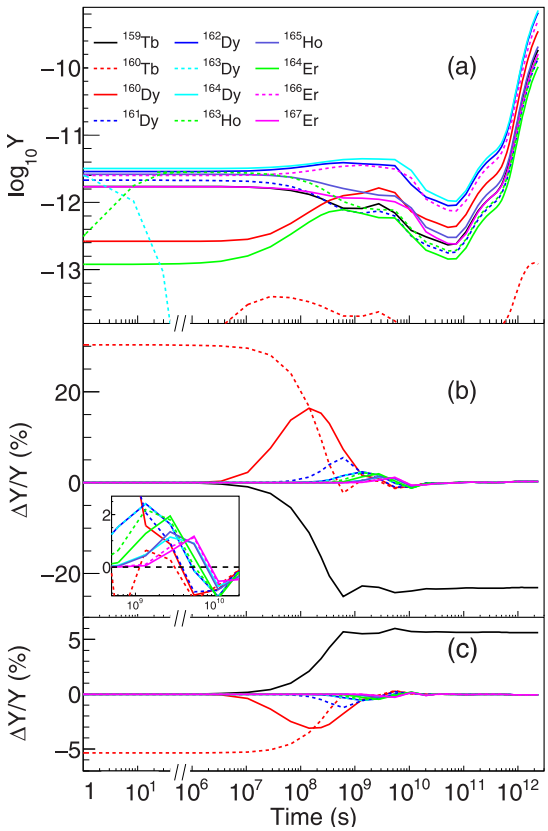

FIG. 7. (Top) Time evolution of nuclear abundances on the test trajectory with $T = 8.9 \times 10^7$ K and $\rho = 7.7 \times 10^3$ g/cm^3. (Middle) The abundance differences between the default case of the JINA REACLIB rate for ^{159}Tb$(n,\gamma)^{160}$Tb, which is derived from KADoNiS-v0.3, and the case of ENDF/B-VIII.0. (Bottom) Same physical quantities as in the middle one but the reaction rates of this work instead of ENDF/B-VIII.0 data are used in calculations.

V. SUMMARY

We measured ^{159}Tb(n,γ) cross sections up to 1 MeV neutron energy by TOF method using the C_6D_6 detectors at the CSNS Back-n facility. Resonance capture kernels are determined from 1 eV to 1.2 keV by analyzing the measured data with the R-matrix code SAMMY. The cross sections are obtained relative to the gold standard over the energy range of 2 keV to 1 MeV and agree well with the TALYS-1.9 theoretical calculations and the JEFF-3.3 evaluation library within the experimental errors. On the other hand, the ENDF/B-VIII.0 evaluated cross section significantly overestimated those of the present study. Maxwellian-averaged neutron capture cross sections (MACS) extracted from the present (n,γ) data are in good agreement with the data of JEFF-3.3 and KADoNiS-v0.3 [17] within 5% and 3%–11% of discrepancies in the whole energy range, respectively. However, the data of ENDF/B-VIII.0 and KADoNiS-v1.0 [19] are significantly overestimated to the present experimental results by 40% and 20%. The sensitivity analysis of the ^{159}Tb$(n,\gamma)^{160}$Tb reaction rate is investigated for the stellar evolution and nucleosynthesis of the $2M_\odot$ star model using the MESA code. Significant changes in the abundances of ^{159,160}Tb, ^{160,161}Dy are observed by comparing the stellar reaction rates of ^{159}Tb$(n,\gamma)^{160}$Tb between KADoNiS-v0.3, this work, and the ENDF/B-VIII.0 evaluation. The present results show very small propagation to the more heavier elements for changing the rate of ^{159}Tb$(n,\gamma)^{160}$Tb because of the establishment of a reaction flow equilibrium between the s-process main component nuclei.

ACKNOWLEDGMENTS

This work was supported by the National Natural Science Foundation of China (Grants No. U2032146, No. 11865010, No. 12175152, No. 11765014, and No. 11609053), Natural Science Foundation of Inner Mongolia (Grants No. 2019JQ01 and 2018MS01009), and the Program for Young Talents of Science and Technology in Universities of Inner Mongolia Autonomous Region (Grant No. NJYT23109). We also thank the efforts of the CSNS Back-n collaboration.

APPENDIX: RESONANCE PARAMETERS

The resonance parameters obtained from fitting the measured capture yield of ^{159}Tb(n,γ) with R-matrix code SAMMY are compared with those from JEFF-3.3 evaluations in Tables VII and VIII. In the energy region from 100 eV to 2 keV, the resonance parameters are not sufficiently reliable due to the worsening of the experimental resolution at the Back-n facility. Therefore, only the resonance energies E_R and capture kernels $k(k = g\Gamma_n\Gamma_\gamma/(\Gamma_n + \Gamma_\gamma)$, ($g$ is the statistical factor) in this energy range are listed in Table VIII. Average resonance parameters, namely, the average level spacing D_l, the neutron strength function S_l, and the average radiation width $< \Gamma_\gamma >_l$, obtained in this work and the recommended data are listed in Table IX. The uncertainties in the tables of this work are from the fitting procedures.

TABLE VII. Resonance parameters up to 100 eV neutron energy for the ^{159}Tb(n, γ) reaction.

J	This work				JEFF-3.3			
	E_R (eV)	Γ_n (meV)	Γ_g (meV)	k	E_R (eV)	Γ_n (meV)	Γ_g Γ_g (meV)	k
2	3.34 ± 0.03	0.34 ± 0.02	102.12 ± 0.06	0.21 ± 0.01	3.360	0.34	103.00	0.21
1	4.97 ± 0.13	0.07 ± 0.05	100.58 ± 0.04	0.03 ± 0.01	4.990	0.08	103.00	0.03
2	11.04 ± 0.03	4.97 ± 0.15	105.45 ± 0.02	2.97 ± 0.10	11.130	7.69	99.00	4.46
1	14.40 ± 0.30	0.12 ± 0.04	95.46 ± 0.08	0.04 ± 0.01	14.500	0.19	105.00	0.07
2	21.19 ± 0.13	1.33 ± 0.18	105.24 ± 0.31	0.82 ± 0.07	21.190	1.14	102.00	0.71
2	24.53 ± 0.07	3.77 ± 0.16	128.35 ± 1.40	2.29 ± 0.09	24.520	5.32	116.00	3.18
2	27.55 ± 0.34	0.48 ± 0.09	95.68 ± 0.85	0.30 ± 0.05	27.510	0.83	102.00	0.52
2	33.83 ± 0.12	3.56 ± 0.58	105.67 ± 0.28	2.15 ± 0.12	33.810	2.61	98.00	1.59
1	40.81 ± 0.63	0.55 ± 0.18	105.78 ± 1.73	0.21 ± 0.06	40.740	0.84	101.00	0.31
2	43.69 ± 0.13	4.33 ± 0.28	103.54 ± 1.25	2.60 ± 0.14	43.630	5.90	97.00	3.48
2	46.04 ± 0.14	7.62 ± 0.52	113.48 ± 1.29	4.46 ± 0.23	45.990	13.94	109.00	7.72
2	50.16 ± 0.24	1.80 ± 0.12	102.86 ± 0.61	1.11 ± 0.10	50.070	1.91	96.00	1.17
2	51.61 ± 0.38	1.13 ± 0.24	98.15 ± 1.02	0.70 ± 0.12	51.550	0.84	96.00	0.52
1	54.08 ± 0.53	0.43 ± 0.12	85.21 ± 1.14	0.16 ± 0.04	53.990	0.83	78.00	0.31
1	57.45 ± 0.36	2.09 ± 0.38	102.48 ± 1.00	0.77 ± 0.10	57.350	2.20	99.00	0.81
2	58.77 ± 0.29	1.38 ± 0.22	98.65 ± 0.79	0.85 ± 0.10	58.630	1.59	96.00	0.98
2	65.17 ± 0.18	7.90 ± 0.54	98.25 ± 1.44	4.57 ± 0.25	65.091	12.61	96.00	6.97
1	66.56 ± 0.39	1.82 ± 0.51	93.22 ± 1.10	0.67 ± 0.13	66.484	3.52	98.00	1.27
1	73.83 ± 0.14	13.02 ± 0.82	102.15 ± 1.30	4.33 ± 0.19	73.665	19.09	98.00	5.99
1	76.45 ± 0.29	7.35 ± 0.98	116.67 ± 2.79	2.59 ± 0.27	76.318	6.92	108.00	2.44
1	77.98 ± 0.37	5.03 ± 0.88	102.14 ± 2.22	1.80 ± 0.24	77.773	7.25	96.00	2.53
1	78.80 ± 0.67	1.06 ± 0.62	95.15 ± 2.00	0.39 ± 0.18	78.598	2.68	85.00	0.97
2	88.44 ± 0.42	3.54 ± 0.66	86.62 ± 1.11	2.13 ± 0.26	88.240	3.37	70.00	2.01
2	90.60 ± 0.33	11.72 ± 1.75	105.68 ± 2.74	6.59 ± 0.67	90.310	6.84	90.00	3.97
1	97.24 ± 0.31	24.37 ± 5.12	118.76 ± 4.77	7.58 ± 0.93	97.004	38.21	101.00	10.40

TABLE VIII. The resonance energies and kernels in this work are compared with the JEFF-3.3 from 100 eV to 1.2 keV.

This work				JEFF-3.3			
E_R (eV)	k	E_R (eV)	k	E_R (eV)	k	E_R (eV)	k
109.24 ± 0.22	8.24 ± 0.34	111.56 ± 0.27	3.04 ± 0.217	108.98	8.19	111.26	2.76
113.89 ± 0.26	6.79 ± 0.472	115.73 ± 0.32	2.25 ± 0.173	113.61	10.66	115.41	3.62
118.83 ± 0.28	2.45 ± 0.225	128.46 ± 0.25	0.63 ± 0.0465	119.06	5.63	128.13	0.53
137.28 ± 0.62	1.28 ± 0.267	138.25 ± 0.45	2.96 ± 0.366	137.43	1.45	137.89	3.57
141.47 ± 0.26	14.80 ± 2.91	143.69 ± 0.26	2.55 ± 0.942	141.16	13.63	143.3	3.98
152.90 ± 0.24	9.67 ± 0.747	155.95 ± 0.28	6.08 ± 0.479	152.52	7.38	155.43	13.48
167.96 ± 0.40	0.83 ± 0.0827	170.13 ± 0.30	3.50 ± 0.258	167.47	0.77	169.63	3.1
173.03 ± 0.38	2.07 ± 0.144	177.21 ± 0.40	6.40 ± 0.447	172.56	1.5	177.3	8.37
186.00 ± 0.53	0.47 ± 0.043	197.78 ± 0.44	6.73 ± 0.414	185.42	0.8	197.36	7.45
200.24 ± 0.48	1.07 ± 0.135	201.84 ± 0.02	0.83 ± 0.439	199.60	1.81	201.37	1.39
211.15 ± 0.54	0.73 ± 0.0579	219.61 ± 0.39	12.13 ± 0.893	210.80	0.71	218.99	28.42
226.33 ± 0.78	0.97 ± 0.109	229.15 ± 1.60	0.41 ± 0.102	225.90	0.79	228.4	0.38
235.67 ± 0.57	15.15 ± 0.928	239.34 ± 0.43	14.12 ± 1.43	235.10	13.25	238.6	11.02
242.17 ± 0.45	5.41 ± 0.516	245.28 ± 0.16	0.15 ± 0.0367	241.43	5.98	244.4	0.47
251.93 ± 0.61	1.90 ± 0.18	254.75 ± 0.58	0.79 ± 0.0953	251.18	3.77	254.1	1.23
263.24 ± 0.71	6.89 ± 0.519	269.05 ± 0.61	5.16 ± 0.329	262.90	10.68	268.39	4.15
273.83 ± 0.58	7.15 ± 0.557	280.05 ± 0.96	1.82 ± 0.341	273.37	13.24	279.8	1.22
281.86 ± 0.69	6.61 ± 0.803	284.77 ± 0.53	17.03 ± 3.04	281.3	6.71	284.14	20.96
290.57 ± 0.59	3.68 ± 0.362	301.43 ± 0.61	16.92 ± 1.03	290.12	6.51	300.76	14.29
306.22 ± 0.65	10.40 ± 0.813	312.88 ± 0.65	14.52 ± 0.968	305.49	9.36	312.11	17.66

TABLE VIII. (*Continued*.)

This work				JEFF-3.3			
E_R (eV)	k	E_R (eV)	k	E_R (eV)	k	E_R (eV)	k
316.27 ± 0.99	1.73 ± 0.322	324.12 ± 1.12	8.25 ± 1.21	315.29	2.12	323.1	6.83
326.58 ± 1.26	10.49 ± 2.57	329.02 ± 0.71	22.49 ± 5.41	325.54	5.41	328.01	19.12
332.86 ± 0.64	21.90 ± 2.48	337.82 ± 0.56	0.13 ± 0.0832	331.94	24.1	336.92	1.08
340.49 ± 0.59	0.18 ± 0.0908	346.16 ± 2.18	12.39 ± 2.49	339.43	0.95	345.28	4.3
348.50 ± 1.58	10.67 ± 3.24	350.83 ± 1.34	4.58 ± 1.19	347.46	13.32	349.88	5.62
358.90 ± 0.78	39.25 ± 2.52	367.32 ± 1.40	10.58 ± 1.54	358.70	29.9	366.32	6.69
370.07 ± 1.79	6.75 ± 2.2	372.77 ± 0.88	22.02 ± 3.26	368.64	3.67	371.81	16.48
375.37 ± 1.21	13.50 ± 2.54	379.40 ± 0.82	18.89 ± 1.62	374.14	11.13	378.16	20.49
385.42 ± 0.82	2.83 ± 0.345	403.20 ± 1.61	8.00 ± 1.55	384.80	3.4	404.5	18.3
409.99 ± 1.22	4.82 ± 0.868	429.98 ± 2.88	0.57 ± 0.218	409.02	6.25	429.1	0.64
433.16 ± 1.11	6.32 ± 0.691	440.26 ± 2.65	10.52 ± 2.66	432.24	6.29	439.96	11.49
442.32 ± 2.07	7.75 ± 3.04	444.97 ± 2.60	5.81 ± 1.58	442.60	9.39	444.45	3.42
451.34 ± 4.06	5.19 ± 2.31	453.39 ± 1.91	10.79 ± 3.73	450.98	1.92	452.8	15.47
455.15 ± 2.46	8.02 ± 3.1	458.69 ± 1.06	9.02 ± 1.2	453.10	3.7	457.7	13.7
463.83 ± 0.02	0.26 ± 0.25	466.15 ± 2.81	2.19 ± 0.846	463.32	1.13	467.87	33.72
475.37 ± 1.47	22.85 ± 2.47	482.73 ± 2.17	3.49 ± 4.38	474.00	12.53	482.07	27.77
489.83 ± 0.87	31.60 ± 5.5	495.58 ± 2.18	10.62 ± 2.69	488.52	37.82	493.97	12.96
499.21 ± 3.03	8.99 ± 2.87	504.15 ± 1.35	13.43 ± 1.6	497.77	6.55	502.96	14.56
511.47 ± 1.65	4.77 ± 0.695	518.43 ± 3.54	5.23 ± 1.87	510.06	12.95	517.37	3.68
521.88 ± 1.58	25.19 ± 2.91	529.19 ± 1.47	17.40 ± 2.07	520.78	21.44	527.79	19.16
533.60 ± 0.88	14.93 ± 2.81	544.84 ± 2.70	4.07 ± 1.42	532.83	18.45	544.5	9.64
547.17 ± 2.92	5.38 ± 1.75	553.36 ± 2.92	8.91 ± 1.85	546.32	1.9	551.8	8.88
558.28 ± 4.99	4.80 ± 2.44	561.60 ± 3.53	12.98 ± 4.92	557.02	7.7	560.47	8.11
566.04 ± 2.01	33.91 ± 5.72	571.47 ± 2.78	10.74 ± 2.55	564.71	16.34	569.73	12.92
576.44 ± 2.79	2.97 ± 1.02	578.42 ± 3.35	4.06 ± 1.49	575.70	4.59	577.39	2.77
581.01 ± 2.24	5.56 ± 1.32	592.31 ± 3.82	23.21 ± 6.52	579.68	14.88	592.39	17.81
594.83 ± 2.48	24.69 ± 8.43	597.47 ± 3.25	16.48 ± 6.58	593.60	35.43	597.52	19.04
600.41 ± 2.16	17.77 ± 5.24	603.10 ± 2.68	9.54 ± 3.21	600.02	11.05	602.71	13.72
605.90 ± 3.19	4.63 ± 1.68	610.50 ± 3.57	16.60 ± 3.29	605.50	2.31	608.12	8.64
615.81 ± 0.94	27.31 ± 9.28	619.30 ± 2.74	7.33 ± 1.91	615.34	50.31	620.49	11.09
627.47 ± 3.03	9.57 ± 3.67	630.28 ± 3.80	17.25 ± 4.37	627.03	22.74	630.29	8.11
639.30 ± 3.02	11.98 ± 2.34	644.79 ± 3.11	11.45 ± 3.57	637.60	8.15	644.28	7.86
649.11 ± 1.49	23.02 ± 5.35	658.22 ± 3.85	1.07 ± 0.358	648.35	31.82	654.5	2.46
660.53 ± 1.76	4.01 ± 0.684	663.24 ± 1.33	4.11 ± 0.636	659.92	8.03	662.6	5.29
678.45 ± 2.51	4.75 ± 1.06	681.88 ± 2.86	7.41 ± 2.1	677.70	4.55	682.51	16.06
684.57 ± 2.23	12.86 ± 2.91	687.71 ± 2.97	18.41 ± 4.44	683.60	34.2	686.64	14.48
694.55 ± 4.29	8.90 ± 2.98	702.00 ± 3.12	15.57 ± 3.21	693.48	7.61	700.57	14.2
708.96 ± 2.52	12.70 ± 2.27	720.87 ± 1.91	8.45 ± 2.84	707.47	6.79	719.68	33.22
723.53 ± 0.40	3.99 ± 2.51	727.88 ± 4.88	3.51 ± 1.75	723.08	1.94	726.97	6.11
732.89 ± 2.91	27.50 ± 4.62	740.27 ± 5.74	6.82 ± 2.59	731.75	25.83	738.5	9.01
748.01 ± 3.48	4.48 ± 1.44	750.91 ± 3.58	4.70 ± 1.61	747.32	7.29	751.46	10.19
754.69 ± 3.68	5.91 ± 1.77	767.45 ± 2.14	57.03 ± 7.81	753.90	5.15	765.2	40.77
768.77 ± 6.80	25.42 ± 22.3	783.42 ± 4.63	6.08 ± 2.81	769.80	19.03	782.5	3.92
787.44 ± 2.68	37.04 ± 8.35	790.76 ± 2.32	21.69 ± 5.76	787.70	28.37	793	6.31
802.50 ± 4.95	12.41 ± 3.37	810.17 ± 5.36	10.99 ± 5.99	802.00	23.45	810.2	16.41
814.44 ± 7.91	15.65 ± 6.87	824.44 ± 2.35	35.91 ± 3.31	815.70	5.22	823.9	22.62
837.62 ± 4.69	2.01 ± 0.792	845.01 ± 3.69	39.72 ± 7.69	837.00	3.88	845.3	25.67
849.34 ± 2.22	31.80 ± 6.76	853.81 ± 3.24	19.32 ± 5.49	850.50	26.82	855.9	6.53
859.26 ± 4.33	8.40 ± 3.06	872.33 ± 19.42	3.24 ± 2.78	861.40	8.88	869.8	4.12
876.21 ± 6.60	14.09 ± 5.05	884.20 ± 4.27	25.68 ± 7.24	875.40	5.39	884.7	21.25
896.76 ± 9.85	6.21 ± 5.75	901.55 ± 3.01	25.35 ± 7	896.40	9.01	901.5	24.29

TABLE VIII. (*Continued.*)

This work				JEFF-3.3			
E_R (eV)	k	E_R (eV)	k	E_R (eV)	k	E_R (eV)	k
994.59 ± 2.90	42.17 ± 6.68	998.76 ± 5.29	24.14 ± 1.07	995.20	43.79	1000.7	20.79
1005.19 ± 78.01	1.36 ± 0.14	1015.76 ± 77.30	6.81 ± 0.68	1005.00	5.74	1016.2	12.62
1028.42 ± 78.92	1.03 ± 1.03	1036.81 ± 78.88	0.28 ± 0.283	1028.00	6.57	1036.3	17.27
1040.66 ± 79.00	0.04 ± 0.0372	1050.39 ± 79.47	0.06 ± 0.0572	1040.20	23.26	1050	33.11
1057.37 ± 79.81	0.03 ± 0.031	1068.11 ± 79.95	4.79 ± 4.76	1057.00	31.37	1067.7	14.64
1097.87 ± 81.84	0.17 ± 0.173	1105.74 ± 82.28	0.31 ± 0.313	1097.60	24.61	1105.5	17.37
1124.31 ± 83.28	0.93 ± 0.929	1132.41 ± 83.67	0.77 ± 0.77	1124.10	20.15	1132.2	21.64
1142.81 ± 85.02	2.98 ± 0.298	1148.20 ± 84.49	0.89 ± 0.888	1142.70	7.42	1148	21.73
1157.19 ± 85.48	10.46 ± 10.5	1172.96 ± 135.74	39.86 ± 46.8	1157.00	13.28	1172.8	51.88
1184.70 ± 87.74	4.23 ± 4.21	1192.36 ± 86.92	1.14 ± 1.14	1184.40	17.68	1192.2	15.7

TABLE IX. Average resonance parameters of this work and the recommended data from Mughabghab [50] and ENDF/B-VIII.0 [51].

Parameters	This work	ENDF/B-VIII.0	S.F. Mughabghab
S_0 (10^{-4})	1.53 ± 0.02	1.207	1.55 ± 0.15
S_1 (10^{-4})	1.83 ± 0.05	1.480	1.86 ± 0.09
S_2 (10^{-4})	1.55 ± 0.21	1.090	1.41 ± 0.24
$\langle\Gamma_\gamma\rangle_0$ (eV)	0.098 ± 0.002	0.097	0.101 ± 0.002
$\langle\Gamma_\gamma\rangle_1$ (eV)	0.055 ± 0.003	0.097	0.050 ± 0.004
$\langle\Gamma_\gamma\rangle_2$ (eV)	0.098	0.097	–

[1] R. Reifarth, C. Lederer, and F. Kappeler, J. Phys. G: Nucl. Part. Phys. **41**, 053101 (2014).
[2] F.-K. Thielemann *et al.*, Prog. Part. Nucl. Phys. **66**, 346 (2011).
[3] E. Burbidge, G. Burbidge, W. Fowler, and F. Hoyle, Rev. Mod. Phys. **29**, 547 (1957).
[4] A. Cameron, Technical Report No. CRLC41, Atomic Energy of Canada Ltd., Chalk River, Ontario, Canada, 1957.
[5] M. Arnould and S. Goriely, Phys. Rep. **384**, 1 (2003).
[6] S. E. Woosley, D. H. Hartmann, R. D. Hoffman, and W. C. Haxton, Astrophys. J. **356**, 272 (1990).
[7] S. Bisterzo *et al.*, Mon. Not. R. Astron. Soc. **418**, 284 (2011).
[8] F. Voss, K. Wisshak, C. Arlandini, F. Käppeler, L. Kazakov, and T. Rauscher, Phys. Rev. C **59**, 1154 (1999).
[9] W. Rapp *et al.*, Astrophys. J. **653**, 474 (2006).
[10] T. Hayakawa *et al.*, Astrophys. J. **685**, 1089 (2008).
[11] R. C. Block *et al.*, in *Proceedings of the EANDC Conference on Time of Flight Method*, Saclay (European Atomic Energy Community, Brussels, 1961), p. 203.
[12] J. H. Gibbons *et al.*, Phys. Rev. **122**, 182 (1961).
[13] J. R. D. Lépine *et al.*, Nucl. Phys. A **196**, 83 (1972).
[14] M. Mizumoto, R. L. Macklin, and J. Halperin, Phys. Rev. C **17**, 522 (1978).
[15] M. Ohkubo, and Y. Kawarasaki, J. Nucl. Sci. Technol. **16**, 701 (1979).
[16] M. Bokhovko *et al.*, in *Nuclear Data for Science and Technology*, edited by S. Qaim (Springer, Berlin, 1992), Vol. 62.
[17] I. Dillmann, R. Plag, F. Kappeler, and T. Rauscher, EFNUDAT fast neutrons: Scientific workshop on neutron measurements, theory applications, JRC-IRMM, available online: www.kadonis.org.
[18] J. Praena *et al.*, Nucl. Data Sheets **120**, 205 (2014).
[19] The Karlsruhe Astrophysical Database of Nucleosynthesis in Stars 1.0 (test version), online at https://exp-astro.de/kadonis1.0/.
[20] N. Dzysiuk *et al.*, Nucl. Phys. A **936**, 6 (2015).
[21] C. Jin-Xiang *et al.*, Nucl. Sci. Tech. **9**, 138 (1998).
[22] C. Guerrero *et al.*, Phys. Rev. Lett. **125**, 142701 (2020).
[23] C. Lederer-Woods *et al.*, Phys. Lett. B **790**, 458 (2019).
[24] C. J. Prokop, A. Couture, S. Jones, S. Mosby, G. Rusev, J. Ullmann, and M. Krtička, Phys. Rev. C **99**, 055809 (2019).
[25] C. Lederer *et al.*, Phys. Rev. Lett. **110**, 022501 (2013).
[26] U. Abbondanno *et al.*, Phys. Rev. Lett. **93**, 161103 (2004).
[27] O. Roig *et al.*, Phys. Rev. C **93**, 034602 (2016).
[28] K. Wisshak, F. Voss, F. Käppeler, and L. Kazakov, Phys. Rev. C **73**, 015807 (2006).
[29] K. Wisshak, F. Voss, F. Käppeler, and G. Reffo, Phys. Rev. C **42**, 1731 (1990).
[30] J. Tang *et al.*, Chin. Phys. C **45**, 062001 (2021).
[31] J. Tang *et al.*, Nuclear Science and Techniques **32**, 11 (2021).
[32] J. Ren *et al.*, Chin. Phys. C **46**, 044002 (2022).
[33] X. X. Li *et al.*, Phys. Rev. C **104**, 054302 (2021).

[34] J. Ren *et al.*, Nucl. Instrum. Methods Phys. Res. A **985**, 164703 (2021).
[35] L. Xie *et al.*, J. Inst. **16**, P10029 (2021).
[36] J. L. Tain *et al.*, J. Nucl. Sci. Technol. **39**, 689 (2002).
[37] U. Abbondanno *et al.*, Nucl. Instrum. Methods Phys. Res. A **521**, 454 (2004).
[38] P. Schillebeeckx *et al.*, Nucl. Data Sheets **113**, 3054 (2012).
[39] Q. Li *et al.*, Nucl. Instrum. Methods Phys. Res. A **946**, 162497 (2019).
[40] Y. Chen *et al.*, Eur. Phys. J. A **55**, 115 (2019).
[41] Q. Wang *et al.*, Rev. Sci. Instrum. **89**, 013511 (2018).
[42] Rene Brun and Fons Rademakers, Nucl. Instrum. Methods Phys. Res. A **389**, 81 (1997); see also https://root.cern/.
[43] R. L. Macklin *et al.*, Nucl. Instrum. Methods **164**, 213 (1979).
[44] A. Borella *et al.*, Nucl. Instrum. Methods Phys. Res. A **577**, 626 (2007).
[45] S. Agostinelli *et al.*, Nucl. Instrum. Methods Phys. Res. A **506**, 250 (2003).
[46] N. M. Larson, Updated users guide for SAMMY: Multilevel R-matrix fits to neutron data using Bayes equations, Report No. ORNL/TM-9179/R8, ENDF-364/R2 (Oak Ridge National Laboratory, 2008).
[47] The Joint Evaluated Fission and Fusion File (JEFF), https://www.oecd-nea.org/dbdata/JEFF33/.
[48] B. Jiang *et al.*, Nucl. Instrum. Methods Phys. Res. A **1013**, 165677 (2021).
[49] F. H. Fröhner, Nucl. Sci. Eng. **103**, 119 (1989).
[50] S. F. Mughabghab, *Atlas of Neutron Resonances*, 6th ed., Resonance Parameters and Thermal Cross Sections (Elsevier, Amsterdam, 2018).
[51] D. A. Brown *et al.*, Nucl. Data Sheets **148**, 1 (2018).
[52] M. Tessler *et al.*, Phys. Lett. B **751**, 418 (2015).
[53] A. J. Koning *et al.*, Nucl. Data Sheets **155**, 1 (2019).
[54] B. Allen, J. Gibbons, and R. Macklin, Adv. Nucl. Phys. **4**, 205 (1971).
[55] S. Goriely, Hauser-Feshbach rates for neutron capture reactions (version 8/29/2005) (2005).
[56] S. Goriely, Hauser-Feshbach rates for neutron capture reactions (version 9/12/2002) (2002).
[57] T. Rauscher and F.-K. Thielemann, At. Data Nucl. Data Tables **75**, 1 (2000).
[58] C. E. Rolfs, W. S. Rodney, *Cauldrons in the Cosmos* (University of Chicago Press, Chicago, 1988).
[59] A. I. Karakas and J. C. Lattanzio, Publ. Astron. Soc. Aust. **31**, e030 (2014).
[60] S. Cristallo *et al.*, Astrophys. J. **696**, 797 (2009).
[61] B. Paxton *et al.*, Astrophys. J. Suppl. Series **192**, 3 (2011).
[62] R. H. Cyburt *et al.*, Astrophys. J. Suppl. Series **189**, 240 (2010).
[63] K. Lodders, Astrophys. J. **591**, 1220 (2003).
[64] R. N. Boyd, G. J. Mathews, and K. Yokoi, Phys. Rev. C **36**, 1522 (1987).
[65] F. Käppeler, R. Gallino, S. Bisterzo, and W. Aoki, Rev. Mod. Phys. **83**, 157 (2011).
[66] A. Koloczek *et al.*, At. Data Nucl. Data Tables **108**, 1 (2016).